Available online at www.sciencedirect.com
SCIENCE DIRECT®
Journal of Electron Spectroscopy and Related Phenomena 141 (2004) 183–193
JOURNAL OF ELECTRON SPECTROSCOPY and Related Phenomena
www.elsevier.com/locate/elspec

Deformation, nuclear motion and fragmentation of core-excited CO_2 probed by multiple-ion coincidence momentum imaging

N. Saito[a,*], Y. Muramatsu[b], H. Chiba[b], K. Ueda[b], K. Kubozuka[c], I. Koyano[c], K. Okada[d], O. Jagutzki[e], A. Czasch[e], T. Weber[e], M. Hattass[e], H. Schmidt-Böcking[e], R. Moshammer[f], M. Lavollée[g], U. Becker[h]

[a] *National Metrology Institute of Japan, AIST, Tsukuba 305-8568, Japan*
[b] *Institute of Multidisciplinary Research for Advanced Materials, Tohoku University, Sendai 980-8577, Japan*
[c] *Department of Material Science, Himeji Institute of Technology, Kamigori, Hyogo 678-1297, Japan*
[d] *Department of Chemistry, Hiroshima University, Higashi-Hiroshima 739-8526, Japan*
[e] *Institut für Kernphsik, Universität Frankfurt, D-60486 Frankfurt, Germany*
[f] *Max-Planck-Institut für Kernphysik, D-67119 Heidelberg, Germany*
[g] *LURE, Bat. 209d, Centre Universitaire Paris-Sud, F-91898, Orsay Cedex, France*
[h] *Fritz-Haber-Institut der Max-Planck-Gesellshaft, D-14195 Berlin, Germany*

Received 9 April 2004; received in revised form 3 June 2004; accepted 8 June 2004
Available online 17 September 2004

Abstract

The nuclear motion and geometry in core-excited CO_2 are probed using a multiple-ion-coincidence imaging technique. We demonstrate that CO_2 has a linear stable geometry in the C/O $1s^{-1}$ core-ionized state and a bent geometry in the C/O $1s^{-1}\pi^*$ core-excited state. The molecules in the C/O $1s^{-1}\pi^*$ A_1 and B_1 Renner–Teller states are probed to be bent in the A_1 state and linear in the B_1 state. The O–O correlation angle distributions are well reproduced using a Coulomb explosion model which takes account of the zero point bending motion in the ground state, the classical bending motion along the potential energy curve of the core-excited state within the core-hole lifetime and the initial inhomogeneous charge distribution in the multiply charged molecular ion just before the dissociation. When the photon energy is tuned to be higher (lower) energy than the $1s^{-1}\pi^*$ resonance center, the events for the $1s^{-1}\pi^*$ A_1 states that result in the low O–O correlation angle distribution are suppressed (enhanced).
© 2004 Elsevier B.V. All rights reserved.

Keywords: Multiple-ion coincidence momentum imaging; CO_2; Nuclear motion; Core-excited state; Molecular deformation; Ionic fragmentation; Coulomb explosion

1. Introduction

In general, when a core electron of a free molecule is excited or ionized, a highly ionized molecular ion is produced after subsequent Auger emission. This molecular ion dissociates into ionic fragments. Dissociation pathways from the core-excited and ionized molecules have been investigated extensively in the last two decades. In the early stage, a photoelectron-photoion coincidence (PEPICO) technique was used for the analysis of the species of the fragment ions from the core-excited and ionized molecules using X-ray line sources [1], electron energy losses [2–4] and synchrotron radiation [5,6]: the electrons were not energetically analyzed and just used as a start signal for the measurement of time-of-flight (TOF) of the ions. One of the most exciting findings by this kind of measurements was that a bond breaking of a core-excited polyatomic molecule often takes place near the excited atomic site [5,7,8]. This site-specific fragmentation was first demonstrated by Eberhardt et al.: they found that only

* Corresponding author. Tel.: +81 298615656; fax: +81 298615673.
E-mail address: norio.saito@aist.go.jp (N. Saito).

0368-2048/$ – see front matter © 2004 Elsevier B.V. All rights reserved.
doi:10.1016/j.elspec.2004.06.007

O^+ ions are produced when the C 1s electron in the CO site in a $(CH_3)_2CO$ molecule is excited to the LUMO π^* [5]. Kinetic energy distributions of fragment ions, which are important to specify the dissociation pathway, were also obtained by analyzing the TOF spectra [9,10]. The photoion–photoion coincidence (PIPICO) technique [11], widely used also for core excitation studies by several groups [12–16], allows one to measure the ion-pair yields and the kinetic energy distributions in the ion-pair formation from the core-excited and ionized molecules. In order to know a state-selected dissociation pathway, however, an energy-resolved Auger electron and ion coincidence technique is demanded [17–21]. The first demonstration of such experiments was performed by Eberhardt et al. for the core-ionized N_2 molecular ions [17].

Angular distributions of fragment ions have also been measured extensively, because such measurements provide the information about the symmetry of the excited states [22–34]. In the case of the $\Sigma \rightarrow \Sigma$ transition in a diatomic molecule, the excitation preferentially occurs when the molecule is parallel to the polarization vector of the incident light (hereafter referred to as the *E* vector). On the other hand, when the molecule is perpendicular to the *E* vector, the molecule is preferentially excited by the $\Sigma \rightarrow \Pi$ transition. If the molecule is assumed to dissociate much faster than its rotation, then the ion angular distribution reflects the direction of molecular orientation in space at the time of excitation [35,36]. The time scales of core-hole decay and subsequent dissociation are of an order of 10^{-14} s, which is much shorter than the time scales of 10^{-12} to 10^{-11} s of the molecular rotation. This requirement of the axial-recoil approximation described above is well fulfilled if there are no long-living intermediate states that cause vibrational structure in the kinetic energy spectra of fragment ions [37]. As a result, the fragment ions energetically ejected after the $\Sigma \rightarrow \Sigma$ and $\Sigma \rightarrow \Pi$ excitations in diatomic molecules are preferentially detected in the direction parallel and perpendicular, respectively, to the *E* vector and thus one can determine the symmetries of core-excited states from the angular distribution measurements of fragment ions. Saito and Suzuki measured the angular distributions of N^+ from the core-excited and core-ionized N_2 molecules using an electron-ion coincidence technique and a rotatable TOF analyzer [22] for the first time. Yagishita et al. [23] measured the angular distributions of fragment ions from N_2 in the N 1s region using a rotatable parallel plate energy analyzer. Symmetry-resolved photoabsorption spectra without selection of ion species from core-excited diatomic molecules can be investigated using two parallel plate energy analyzers [25] and energetic-ion detectors [24,28] mounted at 0° and 90° with respect to the *E* vector. Adachi et al. extended the observations to the linear polyatomic molecules [30]. The extensions to polyatomic molecules with other symmetries, such as C_{2v} and D_{3h}, were also straightforward [26,32,33]. Saito et al. [31] demonstrated that the angular distribution of fragment ions from core-excited CO molecules could nicely be studied by using a multiple-ion coincidence momentum imaging technique with a TOF analyzer and a position sensitive detector. This technique has since turned out to be a powerful tool to investigate nuclear motion in core-excited molecules.

For polyatomic molecules, however, the angular distributions of fragment ions do not always reflect the symmetries of the core-excited electronic states in the point group to which the ground state molecules belong [30,38–40]. Within the lifetime of the order of femtoseconds, the nuclear motion proceeds in the core-excited state [41,42]. In polyatomic molecules, non-totally symmetric nuclear motion may be caused in the core-excited state because the core-excited state may have a stable geometry whose symmetry is different from that of the ground state molecule. This non-totally symmetric nuclear motion breaks the symmetry of the molecule and causes molecular deformation before the Auger decay and subsequent ionic fragmentation occur. In such situations, the ion angular distribution may not reflect the symmetries of the core-excited states before the deformation but may provide the information about the symmetries after the deformation. The molecular deformation in the core-excited state has also been probed by photoelectron-photoion–photoion coincidence (PEPIPICO) technique based on the conventional TOF method [43,44]. The PEPIPICO technique was initially introduced by Eland et al. [45]. The molecular deformation caused by the asymmetric nuclear motion probed in this way is of particular interest because it plays an important role in the decay processes of core-excited molecules and even may open up new dynamical channels unreachable in the initial geometry of the neutral molecule [46,47].

The molecular deformation in the core-excited state is well understood with the help of the equivalent-core $(Z + 1)$ model, combined with the Born–Oppenheimer approximation and the Frank–Condon principle [48–50]. In the equivalent-core model, the molecular excited state in which an inner-shell electron of an atom with the nuclear charge *Z* is promoted to the lowest unoccupied molecular orbital is approximated by the ground state molecule in which the *Z* atom is replaced by the $(Z + 1)$ atom and an electron is added to the valence shell. Analogously, the inner-shell excited Rydberg state and the inner-shell ionized state are approximated by the valence excited Rydberg state of the $(Z + 1)$ molecule and the ground state of the $(Z + 1)$ molecular ion, respectively. Note that the $(Z + 1)$ molecular ion has a geometry of the same symmetry as that of the neutral *Z* molecule while the $(Z+1)$ molecule may have a geometry of different symmetry. For example, the geometry of CO_2 in the ground state is linear [51]. The LUMO is $2\pi_u$. Thus, according to the $(Z + 1)$ model, CO_2 in the C $1s^{-1}2\pi_u$ excited state can be approximated by NO_2 in the ground state. The geometry of NO_2 in the ground state is bent and its O–N–O bond angle is 134.25° [51]. Therefore, the geometry of CO_2 in the C $1s^{-1}2\pi_u$ excited state is expected to be bent also with a bond angle of about 134°. The C 1s ionized CO_2, on the other hand, can be approximated by the ground state NO_2^+ which is known to be linear just as CO_2. The C $1s^{-1}\sigma^*$ excited state, which is located above the C 1s

threshold and forms the shape resonance, is also expected to be linear [29,38,52,53].

The $1s^{-1}\pi^*$ core-excited states of linear triatomic molecules such as CO_2, N_2O, OCS, and CS_2 are in fact doubly degenerate [38,52–56]. Consider here the doubly degenerate core-excited Π state C $1s^{-1}2\pi_u$ Π_u in CO_2. This state splits into two when the nuclear motion takes place along the bending coordinate Q_2. This energy-splitting phenomenon caused by the bending motion is referred to as the Renner–Teller (RT) effect. A schematic representation of the RT states split from C $1s^{-1}2\pi_u$ Π_u is given in Fig. 1. The lower branch of the RT states has a bent stable geometry. This bent state has an electron in the $2\pi_u$ orbital that lies in the bending plane of the molecule, and thus may be called an in-plane state (i.e., A_1 in C_{2v}). The upper branch, on the other hand, remains linear. This linear state has an electron in the π orbital that lies perpendicularly to the bending plane and thus may be called an out-of-plane state (i.e., B_1 in C_{2v}). Referring to the equivalent core model, one can correlate these in-plane and out-of-plane states to the ground and first excited states of NO_2, respectively.

The bent geometry of the molecule in the inner-shell-excited state has previously been probed by an indirect way, i.e., by the measurement of the angular distribution of fragment ions from the core-excited molecules [29,38,40], as discussed above, and of resonant Auger spectroscopy [47,53,56,57]. When the angular distributions of fragment ions of CO_2 are measured at the C/O 1s→π* excitation, it turned out that the Π symmetry did not manifest itself clearly any more in the angular distribution data [29,38,40]. This deterioration of the symmetry dependence was interpreted as the result of the molecule being bent in the core-excited state. The bent geometry, however, has never been probed directly.

Recent rapid developments of multiple ion coincidence momentum imaging techniques invoked renewal of interest in the non-totally symmetric motion and the resulting molecular deformation in the core-excited states, because, with this technique, one can directly probe the non-totally symmetric

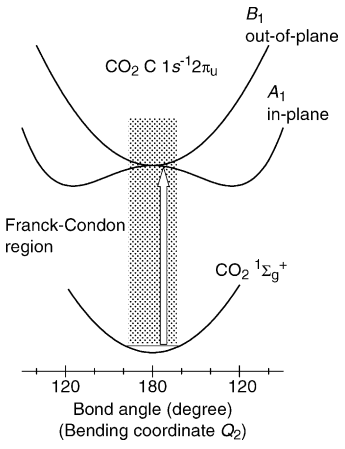

Fig. 1. A schematic representation of the Renner–Teller states split from the C $1s^{-1}2\pi_u$ state of CO_2.

nuclear motion and the molecular deformation in the core-excited states [31,58–64]. This technique is based on the measurements of time-of-flight for all fragment ions using a position-sensitive detector and allows one to extract the complete information about the linear momentum (p_x, p_y, p_z) for each fragment ion.

Let us consider the core-excited CO_2 molecule. One can measure the linear momenta of the three ions C^+, O^+, and O^+ from CO_2^{3+} in coincidence. The triply charged molecular parent ion CO_2^{3+} is produced by the Auger decay of the inner-shell excited states of CO_2. This triply charged molecular ion, representing a few percent of the total ionization yield, has high internal energy and breaks up very rapidly due to the Coulomb explosion. The breakings of the two bonds are simultaneous and the axial-recoil approximation holds [35,36]. Despite the small fraction for the formation of the triply charged parent ions, the linear momenta of the fragment ions reflect the geometry of the molecule at the time when the Coulomb explosion starts because the properties of the excited state are independent of the decay channel. Then we can select the state in which the direction of the bending motion is parallel to the *E* vector of the incident light or the state in which the molecular plane is perpendicular to the *E* vector, by examining the linear momenta of the three fragment ions C^+, O^+, and O^+. Vector correlation among the linear momenta of the three fragment ions thus measured separately for these two states gives us the direct information about the geometries of the RT A_1 and B_1 pair states.

In the present paper, we discuss the nuclear motion and geometry of CO_2 in their inner-shell excited states probed using the multiple ion coincidence momentum imaging technique. The next section describes the experimental apparatus, data processing electronics, and calculation of the ion momenta for investigating symmetry and nuclear dynamics of inner-shell excited molecules. In Section 3, we demonstrate that CO_2 in the C/O $1s^{-1}2\pi_u$ states is bent whereas CO_2 in the C/O $1s^{-1}$ ionized states is linear. Then, we illustrate how to resolve the symmetries of the C/O $1s^{-1}2\pi_u$ inner-shell excited states of the CO_2 molecule, which split into two states, A_1 and B_1, due to the $D_{\infty h} \rightarrow C_{2v}$ symmetry lowering by the Renner–Teller effect. The nuclear motion is discussed in detail in conjunction with a Coulomb explosion model. Changes in the bending motion with the excitation energy in the resonance peak are also discussed.

2. Experiment

The experiments are carried out on the c branch of the soft X-ray photochemistry beamline 27SU at SPring-8 [65,66]. This beamline has a figure-8 undulator as a light source [67]. This undulator provides linearly polarized light whose electric vector is horizontal for the first-order harmonic light and vertical for the 0.5th-order harmonic light. The degree of light polarization is almost perfect on the beam axis for the 0.5th- and first-order lights and deteriorates for the higher

harmonics, higher energies and larger acceptance angles [68]. The polarization degree is better than 0.98 for the 0.5th- and first-order lights with a certain restriction of the acceptance angle at any photon energy. When the front-end-slit is widely opened (a large acceptance angle), the polarization degree at the photon energy of 540 eV deteriorates to about 0.97 for the 0.5th-order light, to about 0.90 for the first-order light, and to about 0.82 for the 1.5th-order light. These values of the polarization degree are measured using the Ne 2s and 2p photoelectrons. The monochromator is of Hettrick type [69]. It has three exchangeable varied line-space plane gratings and covers the photon energy region from 150 eV to 2500 eV [65]. The highest achievable relative resolution is between 10,000 and 20,000, depending on the energy. For example, the values are about 10,000 and 14,000 at the photon energies of 300 eV and 540 eV, respectively. The photon beam is focused to the size less than 0.5 mm high and 0.2 mm wide in the experimental chamber. The experiments are performed using the vertical polarization (0.5th-order light) and the resolution of about 10,000 both in the C 1s and O 1s excitation region.

Fig. 2 shows the multiple ion coincidence momentum imaging apparatus. Multiple ion coincidence momentum imaging technique is based on the time-of-flight (TOF) measurements using a position sensitive TOF spectrometer and a supersonic jet. The TOF and position on the detector of the ion allow one to extract the complete information about the linear momentum (p_x, p_y, p_z) for each ion without ambiguity. A sample gas of CO_2 is introduced into the source point in the form of a supersonic jet and crosses the photon beam perpendicularly. The supersonic jet is produced using a gas nozzle with a hole of 30 μm in diameter and a skimmer with a hole of 300 μm in diameter. The distance between the nozzle and skimmer is adjustable in the range from 6 to 25 mm. The distance between the skimmer and photon beam is fixed to be 50 mm. The lower section of the chamber housing the nozzle is pumped using a 1000 L/s turbo molecular pump. The typical pressure during the experiments is in the order of 10^{-2} Pa in the lower section. The supersonic jet is damped by a cylinder with a hole of 10 mm in diameter equipped with a 300 L/s turbo molecular pump. The upper part of the chamber with the TOF spectrometer is pumped with two 400 L/s turbo molecular pumps. A liquid nitrogen trap is also mounted in the chamber to lower the background pressure. The typical pressure during the experiments is in the order of 10^{-6} Pa.

The TOF axis is fixed perpendicularly to both the light beam and the supersonic jet. The lengths of the acceleration and drift regions for the ion TOF spectrometer are 71 mm and 140 mm, respectively, so as to satisfy the space-focusing condition [70]. Ions are extracted to the right hand side in Fig. 2 with an extraction field of about 20 V/mm and are detected by a multi-channel plate (MCP) of 80 mm effective diameter, followed by a two-dimensional (2D) hexagonal-type delay-line anode (HEX-80, manufactured by Roent-Dek [71]). This three-layer delay-line anode allows us to register position and TOFs of more than two ions in coincidence without suffering from the deadtime intrinsic to the conventional square delay-line anode. Electrons are detected by another MCP of 80 mm effective diameter placed at the opposite end of the accelerating region, followed by a 2D square-type delay-line anode (DLD-80) for other experiments.

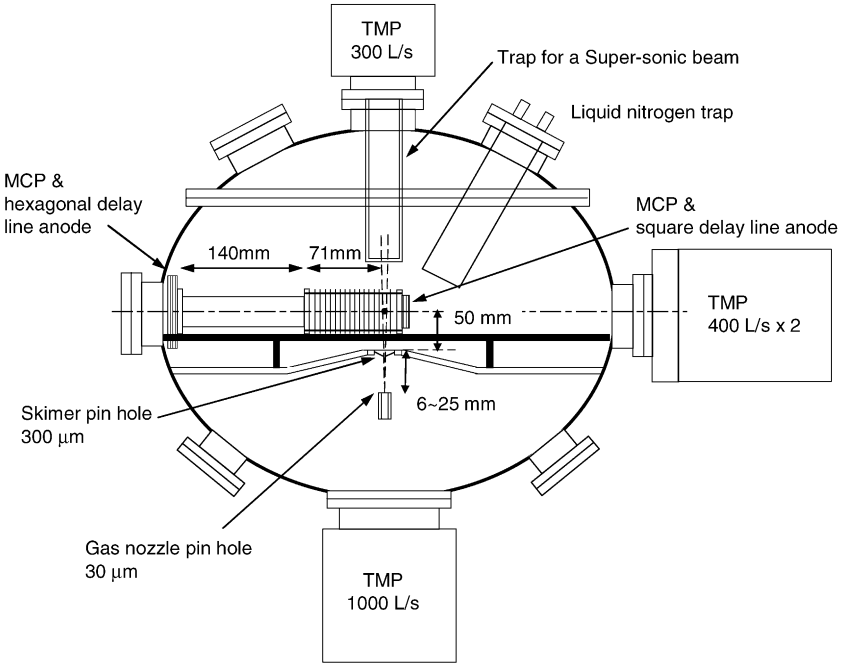

Fig. 2. Illustration of a multiple ion coincidence momentum imaging apparatus.

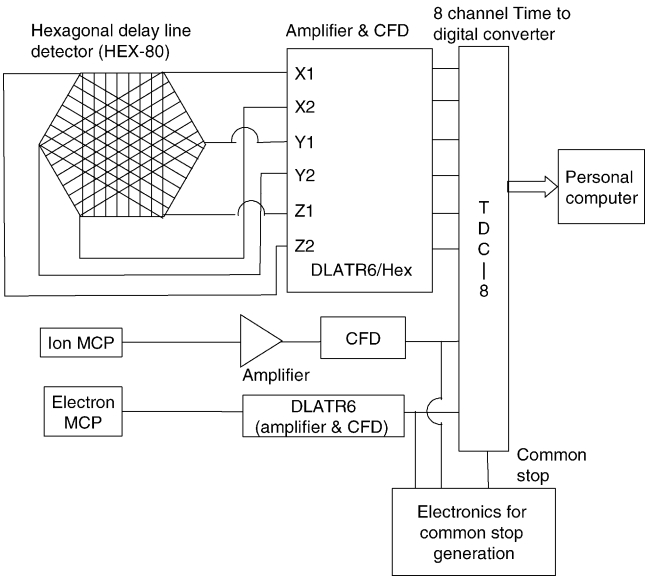

Fig. 3. Schematic diagram of electronics system for recording the TOFs and the positions of ions.

The electronics system for recording the TOFs and positions of ions is schematically illustrated in Fig. 3. There are eight output signals from the spectrometer; six from the delay lines of the HEX-80 delay line anode for ions, one from the MCP for ions and one from the MCP for electrons. The signals from the delay lines are amplified by the differential amplifier and shaped by constant fraction discriminators (CFDs) (RoentDek DLATR6/Hex). The signals from the MCP for ions are amplified by a fast amplifier (Ortec VT120B) and shaped by a CFD (Ortec 935). The signals from the MCP for electrons are amplified by an amplifier and shaped by a CFD (RoentDek DLATR6). These eight shaped signals from CFDs are put into a time-to-digital converter (RoentDek TDC-8) as a start, which has a resolution of 500 ps, a full scale of 32 μs, and 16-fold multi-hit capability. The TDC-8 is operated in a common stop mode. When we detect one electron and two ions at least, a common stop signal is put into the TDC-8. This common stop signal is produced from the electron and ion MCP signals with the combination of fan-in-out (LeCroy 429A), logic unit (LeCroy 622), and gate-and-delay (LeCroy 222) modules.

The data stored in the computer are the times of signals from the delay lines and MCPs. The position of an ion (x, y) on the MCP is calculated from the 6 data from the delay lines. Sometimes it happens that the number of data is less than 6; sometimes some of delay-line signals are detected second even though the ion arrived first at MCP, etc. In order to obtain a correct one-to-one correspondence between a delay line data set and the positions of the ions detected in coincidence, a *resort routine* developed by Czasch [72] is employed. The TOF of the ion, t, is measured as the time difference between the detection times by the electron MCP and ion MCP. The three dimensional momentum of an ion (p_x, p_y, p_z) is calculated by the following equation.

$$p_x = \frac{m(x - x_0)}{t},\ p_y = \frac{m(y - y_0)}{t},\ p_z = qE(t - t_0) \qquad (1)$$

Here, m and q are the mass and charge of the ion, E is the electric field in the acceleration region, t_0 is the averaged TOF of the ion species concerned, and (x_0, y_0) is the center of mass of the position data (x, y). The equation for p_z holds if the Wily–McLaren condition is fulfilled [70] and the electric field is sufficiently high. When all the fragments are detected, the center of mass is given using the momentum conservation law as follows.

$$x_0 = \frac{\sum_i (m_i x_i / t_i)}{\sum_i (m_i / t_i)}, \qquad y_0 = \frac{\sum_i (m_i y_i / t_i)}{\sum_i (m_i / t_i)} \qquad (2)$$

3. Results and discussion

3.1. Proving molecular deformation

The geometry of CO_2 in the C/O $1s^{-1}\pi^*$ state is expected to be bent as described in Introduction. We demonstrate that this is indeed the case, by the measurement of linear momenta, in coincidence, of the three ions, C^+, O^+, and O^+, flying apart from a triply charged molecular ion $CO_2{}^{3+}$ produced via the Auger decay of the C/O $1s^{-1}\pi^*$ state of CO_2. The triply charged molecular ion thus produced has high internal energy and breaks up very rapidly due to the Coulomb explosion. The distribution of the angle between the momenta of the two O^+ ions (i.e., O–O correlation angle) thus reflects the geometry of the molecule at the time when the Coulomb explosion starts.

Fig. 4b and c display ionic triple-fragmentation pattern of the CO_2 measured at the C 1s → $2\pi_u$ (290.7 eV) and C 1s → σ^* (312 eV) resonances, respectively: all the ions ejected to all solid angles were recorded. The angle ϕ denotes the angle between the carbon ion direction and the symmetry axis of the C_{2v} molecule, as illustrated in Fig. 4a. Fig. 4b and c illustrate that the most of fragmentation occurs at the ϕ values of around 0, suggesting that the $CO_2{}^{3+}$ molecular ions dissociate symmetrically (in C_{2v}) and the bonds break simultaneously. The distribution of the O–O correlation angle measured at the C $1s^{-1}\sigma^*$ resonance is peaked at about 162°. This angle actually suggests that the molecule is linear as will be discussed later. The distribution of the O–O correlation angle measured at the C $1s^{-1}2\pi_u$ resonance is, on the other hand, peaked at about 160° and widely spread towards the smaller angles. These findings are consistent with our conjecture that the C $1s^{-1}2\pi_u$ state is bent whereas the ionic C $1s^{-1}$ state followed by the C $1s^{-1}\sigma^*$ state is linear. Note that the C $1s^{-1}\sigma^*$ state emits a photoelectron in a time of the order of atto-seconds before the molecule changes its geometry and thus, the result for the C $1s^{-1}\sigma^*$ resonance reflects the geometry of the C $1s^{-1}$ state.

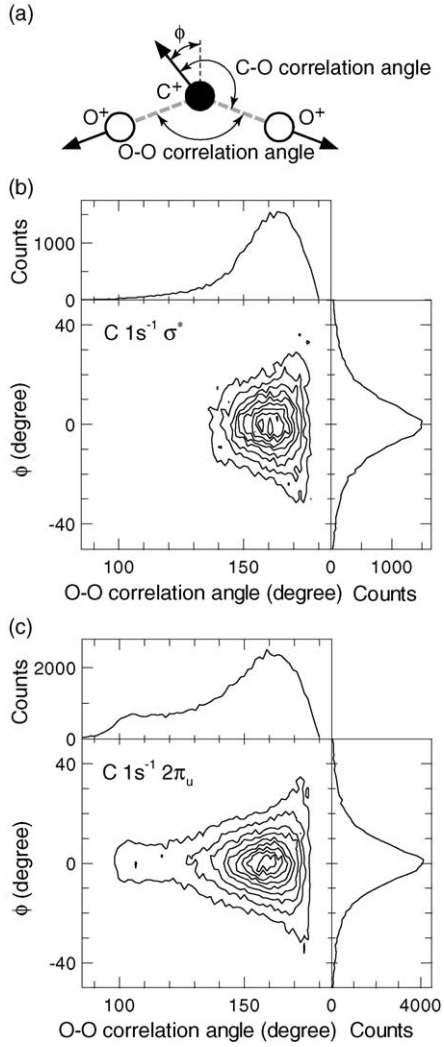

Fig. 4. (a) Geometric configuration of the core-excited CO_2 molecule and CO_2 ionic triple-fragmentation pattern (b) of σ* (312 eV) and (c) of $2\pi_u$ (290.7 eV) detected for all solid angles. The angle ϕ denotes the angle between the carbon ion direction and the symmetric axis of the C_{2v} molecule.

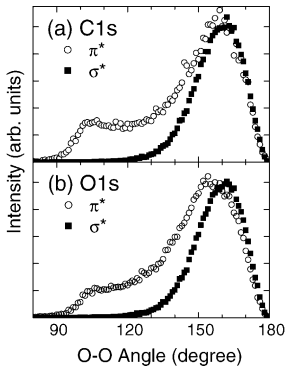

Fig. 5. O—O correlation angle distributions for the ionic triple fragmentation of CO_2^{3+} at the C and O 1s to $2\pi_u$ (open circles) and σ* (closed squares) resonances in all solid angles. Here the O—O correlation angle denotes the angle between the linear momenta of the two O^+ ions obtained by the triple-ion-coincidence momentum imaging technique for the process $CO_2^{3+} \rightarrow C^+ + O^+ + O^+$.

Fig. 5 displays the O–O correlation angle distributions for the ionic triple fragmentation of CO_2^{3+} at the C and O 1s to $2\pi_u$ and σ* resonances. The O–O correlation angle distributions are obtained from the measurements for all solid angles 4π sr and plotted for unit angle θ, integrated over the athimuth angle φ. In order to extract the relative flux per unit solid angle $d\Omega = d\varphi\, d\theta \sin\theta$ from the O–O correlation angle distributions of Fig. 5, one should normalize the signal counts of Fig. 5 by $2\pi \sin\theta$. The reason why the signal counts go down to zero at 180° in Fig. 5 is because of the waiting factor $\sin\theta$ in the present 4π-sr measurements. The O–O correlation distribution measured at the C 1s→σ* resonance is peaked at around 162° and is identical to that at the O 1s→σ* resonance, as well as those at any photon energies in the C/O 1s ionization region (not shown here). The angle of 162° corresponds to about 169° in the distribution of the unit solid angle measurement because of the weight factor $\sin^{-1}\theta$. Note that the O–C–O bond angle can be bent down to 174.7° in the ground state due to the zero-point vibration. If we assume that the Coulomb explosion starts at the linear geometry with this ground-state zero-point distribution, the distribution can be calculated for the O–O angle between the two linear momenta of the two O^+ ions using the Coulomb explosion model suggested in Ref. [73]. It turns out that the peak appears at around 170° in the calculated O–O angle distribution, resulting in good agreement with the observed peak position of 169°. The O–O angle 169° for the peak is smaller than the minimum angle 174.7° because of the long-range Coulomb repulsion with the slowly ejected C^+ ion. The O–O correlation angle distributions for the C $1s^{-1}2\pi_u$ resonances drop to zero around 90°. The interpretation of this angle will be given later.

3.2. Separating Renner–Teller states

So far, we compared the geometry of the core-excited and ionized states of the CO_2 molecule, neglecting the Renner–Teller splitting of the core-excited state. As described in Introduction, the C/O $1s^{-1}2\pi_u$ state of CO_2 actually splits into two along the bending coordinate due to the RT effect [54,55], and the stable geometry of only one of them changes from the linear to bent geometry [38,47,53,56]. The lower branch of the RT states, A_1, becomes bent whereas the upper branch, B_1, remains linear. To probe the geometry of A_1 and B_1 states separately, we propose the following method.

The dipole transition moments from the ground state to the bent A_1 and linear B_1 states are parallel and perpendicular to the direction of the bending motion, respectively. Thus, these two states can be separately observed if the direction of the bending motion can be specified relative to the transition dipole. Fig. 6 illustrates the relation between the polarization vector (E) and the direction of the bending motion. In order to select the A_1 state, we selected the events in which $p(C^+)$ is parallel to E, with the angles between $p(C^+)$ and E smaller

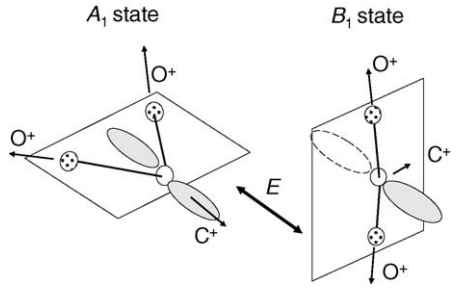

Fig. 6. Relations between the polarization vector of the incident photon and the direction of the bending motion in the C $1s^{-1}2\pi_u$ A_1 and B_1 core-excited states of CO_2.

than 20°. In this way we selected the state in which the direction of the bending motion is parallel to *E*, i.e., the A_1 state. For the selection of the B_1 state, we selected the events in which the vector product of the two linear momenta of the two O^+ ions, $p(O_{(1)}{}^+) \times p(O_{(2)}{}^+)$, is parallel to *E*, with the angles between $p(O_{(1)}{}^+) \times p(O_{(2)}{}^+)$ and *E* smaller than 20°. In this way we selected the state in which the direction of the bending motion is perpendicular to *E*, i.e., the B_1 state. The purities of the A_1 and B_1 states thus selected are estimated to be better than 96 %.

We now focus on the O–O correlation angle distributions for the dissociation starting at the A_1 and B_1 states using the above-described way of selections. Fig. 7a and b displays the O–O correlation angle distributions for the excitation to C $1s^{-1}2\pi_u$ A_1 and B_1 and O $1s^{-1}2\pi_u$ A_1 and B_1, respectively. It is found that the O–O correlation angle distributions for C $1s^{-1}2\pi_u$ B_1 and O $1s^{-1}2\pi_u$ B_1 coincide with each other and also with those for C $1s^{-1}\sigma^*$ and O $1s^{-1}\sigma^*$ in Fig. 5, exhibiting a peak at around 162°. The O–O correlation angle distributions peaking at 162° reflect the dissociation geometry starting at the Condon point where the excitation takes place, i.e., in the Franck–Condon region defined by a zero-point distribution of the linear ground state, as explained above.

The O–O correlation angle distributions for C $1s^{-1}2\pi_u$ A_1 and O $1s^{-1}2\pi_u$ A_1, on the other hand, exhibit a peak at about 160° and extend to lower angles, forming a second peak at around 100°. These two characteristic angles are nearly the same for C $1s^{-1}2\pi_u$ A_1 and O $1s^{-1}2\pi_u$ A_1; only the distributions between these two angles are different. According to the Franck–Condon principle, the molecule is still almost linear immediately after the excitation. Then the molecule starts to bend towards the turning point of the bending motion. The major peak at 160° reflects the dissociation geometry after the spontaneous Auger decay near the Condon point where the excitation takes place. The long tail which extends to 90°, on the other hand, reflects the dissociation geometry after the Auger decay that occurs on the way to the turning point in the C $1s^{-1}2\pi_u$ A_1 and O $1s^{-1}2\pi_u$ A_1 states. The lifetime of the C and O $1s^{-1}2\pi_u$ state is about 7 fs and 3 fs, respectively, whereas the period of the bending vibration is about 46 fs: hence, only a small fraction (≤4%) of the excited molecules can reach the turning point before the Auger decay takes place.

Care should be taken in interpreting the particular angle of about 90° where the O–O correlation angle distribution exhibits a cutoff. At first glance one might think that this angle corresponds to the turning point. Fig. 8 shows the potential energy curves for the C $1s^{-1}2\pi_u$ A_1 and O $1s^{-1}2\pi_u$ A_1 states as a function of the bond angle, calculated using a Hartree–Fock approximation, together with the measured potential energy curve of the ground state of NO_2 [74]. The potential energy curves suggest that the tuning points for the C $1s^{-1}2\pi_u$ A_1 and O $1s^{-1}2\pi_u$ A_1 states are about 110° and 85°, respectively. Thus, in Fig. 7, CO_2 in the C $1s^{-1}2\pi_u$ A_1 state looks more bent than expected and CO_2 in the O $1s^{-1}2\pi_u$ A_1 state looks less bent than expected. It should however be reminded that the O–O correlation angle is not equivalent to the bond angle. In order to correlate the O–O

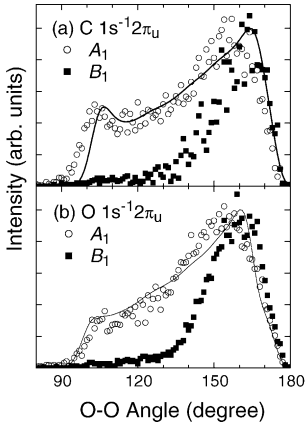

Fig. 7. O–O correlation angle distributions, recorded for 4π-sr measurements, for the excitation to the state with the polarization direction parallel to the bending motion (A_1: open circle) and to the state with the polarization direction perpendicular to the bending motion (B_1: closed square). The solid curves show the calculated distributions for the A_1 state using the Coulomb explosion model. (a) C $1s^{-1}2\pi_u$ and (b) O $1s^{-1}2\pi_u$.

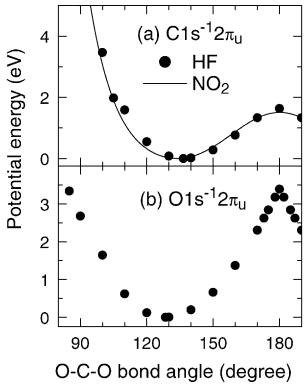

Fig. 8. Potential energy curves for the C $1s^{-1}2\pi_u$ A_1 and O $1s^{-1}2\pi_u$ A_1 states as a function of the bond angle, calculated using a Hartree-Fock approximation, together with the measured potential energy curve of the ground state of NO_2 [74].

correlation angle defined in the momentum space to the bond angle defined by the geometry, one should take account of nuclear dynamics, as we did in the explanation of the O–O correlation angle peaked at 169° for the dissociation of the linear molecule.

3.3. Simplified and improved Coulomb explosion models

Let us calculate the O–O correlation angle distribution for the dissociation from the A_1 state in Fig. 7, first using a *simplified* Coulomb explosion model. The model assumes that the bond lengths are the same as those in the ground state of CO_2, the three atoms in the molecule have the point of single charge, the atoms have no initial velocity, and only the Coulomb forces are exerted among atoms. The zero-point nuclear motion is not taken into account. Then one can calculate the trajectories of three ions by solving the classical equations of motion, Eq. (3), using the Runge–Kutta method.

$$m_1\frac{\mathrm{d}^2\boldsymbol{r}_1}{\mathrm{d}t^2} = \frac{q_1}{4\pi\varepsilon_0}\left(\frac{q_2}{|\boldsymbol{r}_2-\boldsymbol{r}_1|^3}(\boldsymbol{r}_2-\boldsymbol{r}_1) + \frac{q_3}{|\boldsymbol{r}_3-\boldsymbol{r}_1|^3}(\boldsymbol{r}_3-\boldsymbol{r}_1)\right) \quad (3)$$

Here, ε_0 denotes the permittivity of vacuum, m_i, $\boldsymbol{r}_i$, and q_i, denote the mass, the position vector, and the charge of the ion i, respectively. This *simplified* Coulomb explosion model suggests that the bond angles of 110° and 85° correspond to the O–O correlation angles of 122° and 119°, respectively. These values are much larger than the observed minimum angle of about 90° in both the C $1s^{-1}2\pi_u$ A_1 and O $1s^{-1}2\pi_u$ A_1 states. Note that one cannot detect the O–O correlation angle smaller than 119° from the *simplified* Coulomb model because the Coulomb repulsion between the two O^+ ions becomes strong when the bond angle decreases.

These apparent discrepancies can be dissolved by considering the initial inhomogeneous charge distribution in the produced $CO_2{}^{3+}$ molecular ion [75,76] as well as the initial momenta of the ions originating from the zero-point bending motion in the ground state and enhanced bending motion in the excited state. The charges of the triply charged $CO_2{}^{3+}$ molecular ion are initially distributed by +1.52 and +0.74 on C and each of the two O atoms, respectively, according to the Hartree–Fock approximation. As the three ions depart, the charge on each atom approaches unity: the charge on each atom becomes unity when the distance between C and O becomes larger than about 4 Å. The non-equivalent charge distribution is caused by the different electron affinities in the atoms: the electron affinity of the oxygen atom is larger than that of the carbon atom. The repulsion force between the two O atoms becomes smaller by this non-equivalent charge distribution, resulting in the smaller O–O correlation angle than that calculated by the simple Coulomb explosion model. From the above discussion, one can understand that the measured O–O correlation angles do not coincide with the ejection angles when the dissociation takes place.

In order to interpret the measured O–O correlation angles quantitatively, one needs to take account of the effects of the initial momenta of ions, as well as the Coulomb repulsion force among the non-equivalent charge distribution. In the *improved* Coulomb explosion model which takes account of these two effects, the bond angle θ at a time t can be calculated by solving the following equation by the Runge–Kutta method:

$$M\frac{\mathrm{d}^2\theta}{\mathrm{d}t^2} = -\frac{\mathrm{d}V(\theta)}{\mathrm{d}\theta}, \quad (4)$$

where $V(\theta)$ denotes the potential energy curve of the core-excited state of CO_2: the calculated potential energy curves of the core-excited states of CO_2 in Fig. 8 are used. M is the bending inertia and calculated so that the period of the bending vibration becomes 46 fs near the equilibrium bond angle. The initial bond angle θ_0 in the unit of degree and the initial energy of the bond angle $E = M(\mathrm{d}\theta_0/\mathrm{d}t)^2/2$ in the unit of eV are determined by the ground-state zero-point bending vibration and calculated using the following equations with the zero-point energy of 41.3 meV, the maximum bending angle of 174.7° and the random parameter α.

$$\begin{aligned}\theta_0 &= 180 + (180 - 174.7)\sin\alpha \\ E &= 0.0413|\sin\alpha|\end{aligned} \quad (5)$$

During the bending motion, the molecule decays with the lifetime τ. In the calculation, τ = 6.5 fs for C 1s and τ = 3.5 fs for O 1s are used. These values are sufficiently close to the natural core-hole lifetime of 7 fs and 3 fs, respectively, and the results of the calculations agree better with the experiments than using these core-hole lifetime values, as seen below. Then the bond-angle distribution $I(\theta)$ in the excited state can be expressed as

$$I(\theta) = I(\theta_0)\exp\left(\frac{-\tau}{t}\right)$$

After the molecule decays, the trajectories of the departing ions are calculated using Eq. (3) with the inhomogeneous charge distribution. The obtained O–O correlation angle distribution is convoluted with Gaussian of 5° because the experimental angle resolution is expected to be 5°.

The results of the simulation, given in Fig. 7 by the solid curves, show reasonable agreements with the experimental results. The difference in the O–O correlation distributions between the C 1s and O 1s states can be attributed to both the difference in the depth of the potential energy surface and in the lifetime, i.e., about 6.5 fs for C 1s and 3.5 fs for O 1s. The lifetime of 3.5 fs would show much low counts for the low O–O correlation angles if the potential energy surface for the O 1s excited state was the same as that for the C 1s excited state. When the potential energy surface is steep, the molecule is forced to be bent and then the probability for the molecule with a low O–O correlation angle becomes high even in the short lifetime.

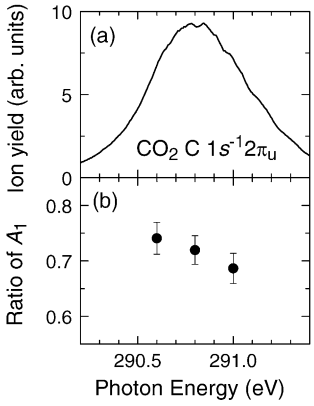

Fig. 9. (a) Ion yield spectrum and (b) intensity ratios between the A_1 and the sum of the A_1 and B_1 states in the C 1 C $1s^{-1}2\pi_u$ excitation.

3.4. Detuning effects

Figs. 9a and 10a show the ion yield spectra of CO_2 in the C and O 1s → $2\pi_u$ excitation regions, respectively. Both spectra have a broad feature due to the vibrational excitations. Progression of the symmetric stretching vibration is seen on the higher energy side of the C 1s → $2\pi_u$ excitation region in Fig. 9a. In Fig. 10a, the O 1s → 3s excitation overlaps on the higher energy side of the O 1s → $2\pi_u$ excitation region. From the schematic potential energy diagram of the RT states, it is clear that the ratio of the A_1 excitation decreases with the increase in the excitation photon energy. Figs. 9b and 10b illustrate the variation of the intensity ratios between A_1 and the sum of A_1 and B_1 for the C $1s^{-1}2\pi_u$ and O $1s^{-1}2\pi_u$ excitations as a function of excitation energy. The ratios for the excitation at the top of the resonances range from 0.57 to 0.74. These ratios are almost the same as those for the corresponding N_2O transitions [63]. The ratios decrease with the increase in the excitation photon energy.

On the basis of the Franck–Condon principle, the bond angle of the molecule in the A_1 state at the instance of excitation is expected to be smaller (larger) with the decrease (increase) in the excitation energy. The different initial geometries should cause different nuclear motions in the core-excited states and result in different O–O correlation angles. Fig. 11 shows the O–O correlation angle distributions for the CO_2 molecule in the C $1s^{-1}2\pi_u$ A_1 state measured at 290.6, 290.8, and 291.0 eV and in O $1s^{-1}2\pi_u$ A_1 measured at 534.8 and 535.4 eV. The events of the lower O–O correlation angles are suppressed (enhanced) for the higher (lower) photon energy of 291.0 eV (290.6 eV) compared to those for the center of the resonance at 290.8 eV. The same tendency can be seen also for the O 1s excitation. These findings suggest that the molecule in the A_1 state excited with the higher photon energy is indeed less bent than that excited by the lower photon energy.

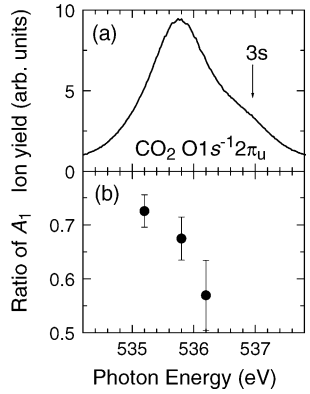

Fig. 10. (a) Ion yield spectrum and (b) intensity ratios between the A_1 and the sum of the A_1 and B_1 states in the O $1s^{-1}2\pi_u$ excitation.

The slope of the potential energy surface determines the force for the nuclear motion in the core-excited states and thus affects the O–O correlation angle distributions. The excitation at higher energies occurs into the larger bond angles, where the slope of the potential energy surface along the bending Q_2 coordinate is almost flat. On the other hand, when the molecule is excited with lower photon energies, the bond angle is smaller than that for higher photon energies and the slope of the potential energy surface is steeper. The *improved* Coulomb explosion model, which takes account of the initial geometry and nuclear motion as well as inhomogeneous Coulomb repulsion as described earlier, indeed explain the dependence of the O–O correlation angle distribution on the detuning. The solid curves in Fig. 11 show the calculated O–O correlation angle distributions. The bond angle at the instant of excitation is near 180° for higher photon energy and 176° for lower photon energy. Reasonably good agreement is seen between the calculated and measured distributions, suggesting the validity of the *improved* Coulomb explosion model. Similar detuning effect is also seen in the Nt(terminal N)–O correlation angles for N_2O at the Nt, Nc(central N), and O $1s^{-1}3\pi$ excitation [63].

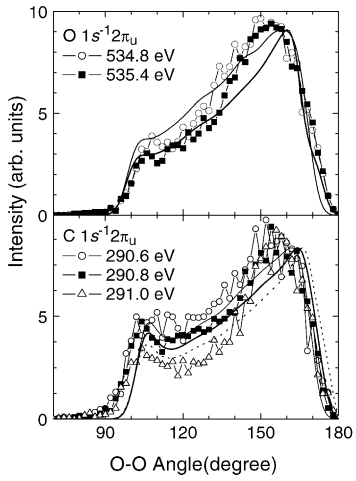

Fig. 11. O–O correlation angle distributions of CO_2 molecules in the C $1s^{-1}2\pi_u$ A_1 states measured at the photon energies of 290.6 (open circle), 290.8 (closed square), and 291.0 eV (open triangle) and in O $1s^{-1}2\pi_u$ A_1 measured at the photon energies of 534.8 (open circle) and 535.4 eV (closed square). The curves are obtained by the calculation using the Coulomb explosion model (see text).

4. Conclusions

Nuclear motion and geometry of CO_2 in the core-excited states are probed using the triple-ion-coincidence momentum imaging technique. The measured O–O correlation angles do not coincide with the ejection angles when the dissociation takes place. However, when the effects of the initial momenta of atoms and the Coulomb repulsion force with the inhomogeneous charge distribution are taken into account, one can still extract the information about the nuclear motion and geometry in the core-excited state. While CO_2 in the C/O $1s^{-1}\pi^*$ excited states is bent, CO_2 in the C/O $1s^{-1}$ ionized states is linear. The degenerated C/O $1s^{-1}\pi^*$ excited states are split into the A_1 and B_1 states as the bending motion proceeds. The molecules in C/O $1s^{-1}\pi^*$ A_1 and B_1 states are probed to be bent and linear, respectively. The O–O correlation angle distributions in the C/O $1s^{-1}\pi^*$ A_1 states are reproduced using the *improved* Coulomb explosion model proposed here. The distributions depend on the potential energy surface of the core-excited states and the core-hole lifetime. Besides, the initial zero-point bending motion in the ground state in CO_2 and inhomogeneous charge distribution in the CO_2^{3+} after the Auger decay are also found to be important. When the photon energy is detuned to be higher than the resonance center, the O–O correlation angle distributions for the C/O $1s^{-1}\pi^*$ A_1 states show the low intensity at the lower angles. On the other hand, the O–O correlation angle distributions for the lower photon energy than the resonance center increase in the lower angles. These suggest that the slope of the potential energy surface at the excitation and the initial bending motion affect the O–O correlation angle distributions. It is also found that the ratios of the C/O $1s^{-1}\pi^*$ A_1 states decrease as the photon energy is increased within the resonance peak.

Acknowledgements

The experiments were performed at SPring-8 with the approval of the program review committee. The work was partially supported by the Grants-in-Aid for Scientific Research (B) from Japan Society for Promotion of Science and by the Budget for Nuclear Research of Ministry of Education, Culture, Sports, Science and Technology, based on the screening and counseling by the Atomic Energy Commission. The authors are grateful to the staff of SPring-8, especially Drs. H. Ohashi and Y. Tamenori, for their help in the course of the experiments.

References

[1] T.A. Carlson, M.O. Krause, J. Chem. Phys. 56 (1972) 3206.
[2] M.J. Van der Wiel, Th.M. El-Sherbini, Physica (Utrecht) 59 (1972) 453.
[3] R.B. Kay, Ph.E. Van der Leeuw, M.J. Van der Wiel, J. Phys. B 10 (1977) 2521.
[4] A.P. Hitchcock, C.E. Brion, M.J. van der Wiel, Chem. Phys. Lett. 66 (1979) 213.
[5] W. Eberhardt, T.K. Sham, R. Carr, S. Krummacher, M. Strongin, S.L. Weng, D. Wesner, Phys. Rev. Lett. 50 (1983) 1038.
[6] W. Eberhardt, J. Stöhr, J. Feldhous, E.W. Plummer, F. Sette, Phys. Rev. Lett. 51 (1983) 2370.
[7] S. Nagaoka, I. Koyano, K. Ueda, E. Shigemasa, Y. Sato, A. Yagishita, T. Nagata, T. Hayaishi, Chem. Phys. Lett. 154 (1989) 363.
[8] R. Thissen, M.-J. Hubin-Franskin, M. Furlan, J.-L. Piette, P. Morin, I. Nenner, Chem. Phys. Lett. 199 (1992) 102.
[9] N. Saito, I.H. Suzuki, Int. J. Mass Spectrosc. Ion Process. 82 (1988) 61.
[10] K. Ueda, Y. Sato, S. Nagaoka, A. Yagishita, T. Hayaishi, Chem. Phys. Lett. 170 (1990) 389.
[11] G. Dujardin, S. Leach, O. Dutuit, P.M. Guyon, M. Richard-Viard, Chem. Phys. 88 (1984) 339.
[12] P. Morin, G.G.B. Desouza, I. Nenner, P. Lablanquie, Phys. Rev. Lett. 56 (1986) 131.
[13] A.P. Hitchcock, P. Lablanquie, P. Morin, E.L.A. Lugrin, M. Simon, P. Thiry, I. Nenner, Phys. Rev. A 37 (1988) 2448.
[14] N. Saito, I.H. Suzuki, J. Phys. B 20 (1987) L785;
N. Saito, I.H. Suzuki, J. Chem. Phys. 91 (1989) 5329.
[15] K. Ueda, E. Shigemasa, Y. Sato, S. Nagaoka, I. Koyano, A. Yagishita, T. Nagata, T. Hayaishi, Chem. Phys. Lett. 154 (1989) 357.
[16] T. Imamura, C.E. Brion, I. Koyano, T. Ibuki, T. Masuoka, J. Chem. Phys. 94 (1991) 4936.
[17] W. Eberhardt, E.W. Plummer, I.W. Lyo, R. Carr, W.K. Ford, Phys. Rev. Lett. 58 (1987) 207.
[18] D.M. Hanson, C.I. Ma, K. Lee, D. Lapiano-Smith, D.Y. Kim, J. Chem. Phys. 93 (1990) 9200.
[19] K. Ueda, H. Chiba, Y. Sato, T. Hayaishi, E. Shigemasa, A. Yagishita, Phys. Rev. A 46 (1992) 5.
[20] C. Miron, M. Simon, N. Leclercq, D.L. Hansen, P. Morin, Phys. Rev. Lett. 81 (1998) 4104.
[21] E. Kukk, J.R.I. Riu, M. Stankiewicz, P.A. Hatherly, P. Erman, E. Rachlew, P. Winiarczyk, M. Huttula, S. Aksela, Phys. Rev. A 66 (2002) 012704.
[22] N. Saito, I.H. Suzuki, Phys. Rev. Lett. 61 (1988) 2740.
[23] A. Yagishita, H. Maezawa, M. Ukai, E. Shigemasa, Phys. Rev. Lett. 62 (1989) 36.
[24] K. Lee, D.Y. Kim, C.I. Ma, D.A. Lapiano-Smith, D.M. Hanson, J. Chem. Phys. 93 (1990) 7936.
[25] E. Shigemasa, K. Ueda, Y. Sato, T. Sasaki, A. Yagishita, Phys. Rev. A 45 (1992) 2915.
[26] D.Y. Kim, K. Lee, C.I. Ma, M. Mahalingam, D.M. Hanson, S.L. Hulbuert, J. Chem. Phys. 97 (1992) 5915.
[27] O. Hemmers, F. Heiser, J. Eiben, R. Wehliz, U. Becker, Phys. Rev. Lett. 71 (1993) 987.
[28] A. Yagishita, E. Shigemasa, N. Kosugi, Phys. Rev. Lett. 72 (1994) 3961.
[29] J.D. Bozek, N. Saito, I.H. Suzuki, Phys. Rev. A 51 (1995) 4563.
[30] J. Adachi, N. Kosugi, E. Shigemasa, A. Yagishita, J. Chem. Phys. 102 (1995) 7369.
[31] N. Saito, F. Heiser, O. Hemmers, K. Wieliczek, J. Viefhaus, U. Becker, Phys. Rev. A 54 (1996) 2004.
[32] Y. Shimizu, K. Ueda, H. Chiba, M. Okunishi, K. Ohomori, J.B. West, Y. Sato, T. Hayaishi, J. Chem. Phys. 107 (1997) 2415, 2419.
[33] K. Okada, K. Ueda, T. Tokushima, Y. Senba, H. Yoshida, Y. Shimizu, M. Simon, H. Chiba, H. Okumura, Y. Tamenori, H. Ohashi, N. Saito, S. Nagaoka, I.H. Suzuki, E. Ishiguro, I. Koyano, T. Ibuki, A. Hiraya, Chem. Phys. Lett. 326 (2000) 314.
[34] M. Simon, C. Miron, P. Morin, in: J. Ullrich, V. Shevelko (Eds.), Series on Atomic, Optical and Plasma Physics, 35, Springer Verlag, Heidelberg, 2003, pp. 283–301.
[35] R.N. Zare, Mol. Photochem. 4 (1972) 1.
[36] G.E. Busch, K.R. Wilson, J. Chem. Phys. 56 (1972) 3638.

[37] Th. Weber, O. Jagutzki, M. Hattass, A. Staudte, A. Nauert, L. Schmidt, M.H. Prior, A.L. Landers, A. Bräuning-Demian, H. Bräuning, C.L. Cocke, T. Osipov, I. Ali, R. Díez Muiño, D. Rolles, F.J. García de Abajo, C.S. Fadley, M.A. Van Hove, A. Cassimi, H. Schmidt-Böcking, R. Dörner, J. Phys. B 34 (2001) 3669.
[38] J. Adachi, N. Kosugi, E. Shigemasa, A. Yagishita, J. Chem. Phys. 107 (1997) 4919.
[39] K. Ueda, Y. Shimizu, H. Chiba, M. Okunishi, K. Ohmori, J.B. West, Y. Sato, T. Hayaishi, H. Nakamatsu, T. Mukoyama, Phys. Rev. Lett. 79 (1997) 3371.
[40] N. Saito, K. Ueda, M. Simon, K. Okada, Y. Shimizu, H. Chiba, Y. Senba, H. Okumura, H. Ohashi, Y. Tamenori, S. Nagaoka, A. Hiraya, H. Yoshida, E. Ishiguro, T. Ibuki, I.H. Suzuki, I. Koyano, Phys. Rev. A 62 (2000) 042503.
[41] P. Morin, I. Nenner, Phys. Rev. Lett. 56 (1986) 1913.
[42] I. Hjelte, M.N. Piancastelli, R.F. Fink, O. Björneholm, M. Bässler, R. Feifel, A. Giertz, H. Wang, K. Wiesner, A. Ausmees, C. Miron, S.L. Sorensen, S. Svensson, Chem. Phys. Lett. 334 (2001) 151.
[43] T. LeBrun, M. Lavollée, M. Simon, P. Morin, J. Chem. Phys. 98 (1993) 2534.
[44] M. Simon, M. Lavollée, M. Meyer, P. Morin, J. Electron Spectrosc. Relat. Phenom. 79 (1996) 401.
[45] J.H.D. Eland, F.S. Wort, R.N. Royds, J. Electron. Spectrosc. 41 (1986) 297.
[46] K. Ueda, M. Simon, C. Miron, N. Leclercq, R. Guillemin, P. Morin, S. Tanaka, Phys. Rev. Lett. 83 (1999) 3800.
[47] P. Morin, M. Simon, C. Miron, N. Leclercq, E. Kukk, J.D. Bozek, N. Berrah, Phys. Rev. A 61 (2000) 050701.
[48] M. Nakamura, M. Sasanuma, S. Sato, M. Watanabe, H. Yamashita, Y. Iguchi, A. Ejiri, S. Nakai, S. Yamagushi, T. Sagawa, Y. Nakai, T. Oshio, Phys. Rev. 178 (1969) 80.
[49] M. Tronc, G.C. King, F.H. Read, J. Phys. B 12 (1979) 137.
[50] C.T. Chen, Y. Ma, F. Sette, Phys. Rev. A 40 (1989) 6737.
[51] A.A. Radzig, B.M. Smirnov, Reference Data on Atoms, Molecules and Ions, Springer-Verlag, Berlin, 1985, p. 417.
[52] G.R. Wight, C.E. Brion, J. Electron. Spectrosc. Relat. Phenom. 3 (1973) 191.
[53] E. Kukk, J.D. Bozek, N. Berrah, Phys. Rev. A 62 (2000) 032708.
[54] G. Herzberg, Infrared and Raman Spectra of Polyatomic Molecules, Van Nostrand, New York, 1973.
[55] H. Köppel, W. Domcke, L.S. Cederbaum, Adv. Chem. Phys. 57 (1984) 59.
[56] Y. Muramatsu, Y. Shimizu, H. Yoshida, K. Okada, N. Saito, I. Koyano, H. Tanaka, K. Ueda, Chem. Phys. Lett. 330 (2000) 91.
[57] C. Miron, M. Simon, P. Morin, J. Chem. Phys. 115 (2001) 1.
[58] M. Lavollée, V. Brems, J. Chem. Phys. 110 (1999) 918.
[59] Y. Muramatsu, K. Ueda, N. Saito, H. Chiba, M. Lavollée, A. Czasch, T. Weber, O. Jagutzki, H. Schmidt-Böcking, R. Moshammer, U. Becker, K. Kubozuka, I. Koyano, Phys. Rev. Lett. 88 (2002) 133002.
[60] Y. Muramatsu, K. Ueda, H. Chiba, N. Saito, M. Lavollée, A. Czasch, T. Weber, O. Jagutzki, H. Schmidt-Böcking, R. Moshammer, K. Kubozuka, I. Koyano, Surf. Rev. Lett. 9 (2002) 93.
[61] N. Saito, K. Ueda, I. Koyano, AIP Conference Proceedings 652 (2003) 172.
[62] A. De Fanis, N. Saito, M. Machida, K. Okada, H. Chiba, A. Cassimi, R. Dörner, I. Koyano, K. Ueda, Phys. Rev. A 69 (2004) 022506.
[63] M. Machida, M. Lavollée, J. Randrianjafisoa, G. Laurent, M. Nagoshi, K. Okada, I. Koyano, N. Saito, J. Chem. Phys. 120 (2004) 3635.
[64] N. Saito, A. De Fanis, I. Koyano, K. Ueda, Physica Scripta T110 (2004) 90.
[65] H. Ohashi, E. Ishiguro, Y. Tamenori, H. Okumura, A. Hiraya, H. Yoshida, Y. Senba, K. Okada, N. Saito, I.H. Suzuki, K. Ueda, T. Ibuki, S. Nagaoka, I. Koyano, T. Ishikawa, Nucl. Instrum. Methods A 467/468 (2001) 533.
[66] I. Koyano, M. Okuyama, E. Ishiguro, A. Hiraya, H. Ohashi, T. Kanashima, K. Ueda, I.H. Suzuki, T. Ibuki, J. Synchrotron Radiat. 5 (1998) 545.
[67] T. Tanaka, H. Kitamura, Nucl. Instrum. Methods A 364 (1995) 368; T. Tanaka, H. Kitamura, J. Synchrotron Radiat. 3 (1996) 47.
[68] H.Yoshida, Y. Senba, M. Morita, T. Goya, A. De Fanis, N. Saito, K. Ueda, Y. Tamenori, H. Ohashi, AIP Conference Proceedings.
[69] M.C. Hettrick, S. Bowyer, Appl. Opt. 22 (1983) 3921.
[70] W.C. Wiley, I.H. McLaren, Rev. Sci. Instrum. 26 (1955) 1150.
[71] See http://www.roentdek.com/ for details on the detectors.
[72] A. Czasch, private communication.
[73] U. Ankerhold, B. Esser, F. von Busch, J. Phys. B 30 (1997) 1207.
[74] S.A. Tashkun, P. Jensen, J. Mol. Spectrosc. 165 (1994) 173.
[75] S. Hsieh, J.H.D. Eland, J. Chem. Phys. 103 (1995) 1006.
[76] I. Nenner, P. Morin, in: U. Becker, D.A. Shirley (Eds.), VUV and Soft X-Ray Photoabsortion, Plenum, New York, 1996, pp. 291–354.